Nanoscale

PAPER

View Article Online
View Journal | View Issue

Cite this: *Nanoscale*, 2025, **17**, 8192

A comparative study of bulk and surface W-doped high-Ni cathode materials for lithium-ion batteries†

Gulzat Nuroldayeva,[a,b] Tanay Umurzak,[a,c] Aziza Kireyeva,[a,c] Assylzat Aishova,[a,d] Orynbassar Mukhan,[e] Sung-Soo Kim,[e] Zhumabay Bakenov *[a,c,f] and Nurzhan Umirov *[a,f]

This study explores the influence of tungsten (W) doping on the structural and electrochemical performance of high-nickel $LiNi_{0.8}Co_{0.1}Mn_{0.1}O_2$ (NCM811) cathode materials, aiming to enhance lithium-ion battery high rate and long-term cycling stability. Tungsten was incorporated through two distinct approaches: bulk doping *via* a wet-chemical co-precipitation method and surface doping *via* solid-state processing during calcination. Comprehensive characterization, including X-ray diffraction, scanning electron microscopy, and micro-cavity electrode electrochemical measurements was conducted to elucidate the effect of W doping on the morphology, crystallinity, and lithium-ion transport properties. Results indicate that W doping enhances charge transfer kinetics and stabilizes the NCM811 microstructure, effectively reducing capacity fade. Notably, surface-doped samples (s-LNCMW) demonstrated superior cycling stability, with 92% capacity retention after 500 cycles, attributed to the formation of a protective Li_xWO_y layer. This study provides insights into the optimization of doped NCM cathodes, underscoring the potential of surface tungsten doping as a strategic approach for developing high-energy-density cathodes with improved cycle life for next-generation lithium-ion batteries.

Received 9th November 2024,
Accepted 4th February 2025

DOI: 10.1039/d4nr04691a

rsc.li/nanoscale

1. Introduction

The development of high-energy-density lithium-ion batteries (LIBs) is essential for advancing electric vehicles (EVs) and portable electronic devices.[1,2] Among various cathode materials, nickel-rich layered oxides, such as $LiNi_{0.8}Co_{0.1}Mn_{0.1}O_2$ (NCM811), have gained significant attention. This is due to their high specific capacity, relatively low cost, and satisfactory thermal stability. However, the widespread use of these materials in practical applications is often impeded by issues such as capacity fading, structural instability, and electrolyte decomposition, particularly at the high voltages required to achieve greater energy densities.[3]

The primary drawback of increasing capacity (*i.e.*, deeper delithiation) is the reduced structural stability, which leads to rapid chemo-mechanical deterioration across multiple scales and, ultimately, capacity fading.[4] Two key factors contribute to the degradation of nickel-rich NCM during cycling. First, structural changes caused by the loss of lattice oxygen form a solid, rocksalt-like layer on the particle surface, which impedes lithium passage and causes nickel to become electrochemically inactive, with a growing fraction of Ni^{2+} approaching NiO stoichiometry.[5,6] Second, anisotropic changes in unit-cell volume, particularly a decrease in the c lattice parameter during the H2/H3 phase transition, create fractures and ultimately result in the fragmentation of secondary particles, exposing more reactive surface area.[7,8]

Doping strategies have been extensively studied to address the challenges associated with NCM (nickel–cobalt–manganese) cathodes, such as stabilizing crystal structures, reducing cation mixing, and improving electrochemical performance.[9] Tungsten (W) doping, in particular, has demonstrated significant potential in enhancing the structural and electrochemical properties of NCM materials.[10] The incorporation of W^{6+} ions

[a]*Institute of Batteries, LLC, Kabanbay Batyr Ave 53, Astana 010000, Kazakhstan. E-mail: nurzhan.umirov@nu.edu.kz*
[b]*Department of Chemistry, Nazarbayev University, Kabanbay Batyr Ave 53, Astana 010000, Kazakhstan*
[c]*Department of Chemical and Materials Engineering, Nazarbayev University, Kabanbay Batyr Ave 53, Astana 010000, Kazakhstan. E-mail: zbakenov@nu.edu.kz*
[d]*Department of Process Engineering and Applied Science, Dalhousie University, Halifax, Nova Scotia B3H 4R2, Canada*
[e]*Graduate School of Energy Science and Technology, Chungnam National University, Yuseong-gu, Daejeon 34134, Republic of Korea*
[f]*Center for Energy and Advanced Materials Science, National Laboratory Astana, Kabanbay Batyr Ave 53, Astana 010000, Kazakhstan*

† Electronic supplementary information (ESI) available. See DOI: https://doi.org/10.1039/d4nr04691a

can improve the structural integrity of the cathode by reinforcing the transition metal (TM) layer and suppressing phase transitions during cycling. Additionally, W doping has been reported to reduce the formation of microcracks, a common issue in high-Ni cathodes, thus improving overall cycling stability.[11,12]

However, the effects of different doping methods—specifically bulk *versus* surface doping—on the performance of NCM cathodes remain underexplored. Bulk doping involves integrating dopants throughout the material, which can lead to uniform enhancements in structural properties.[13] In contrast, surface doping or coating can help mitigate reactions at the surface, reduce electrolyte decomposition, and create a protective layer against structural degradation during repeated lithium intercalation and deintercalation.

This study aims to conduct a comparative analysis of bulk and surface W-doped cathode materials, specifically NCM811, synthesized using wet and solid-state methods. The primary focus is on understanding how these doping strategies influence the microstructure, surface characteristics, and electrochemical performance of the cathode materials. By systematically investigating the role of W doping, this research seeks to provide insights into optimizing the design of high-Ni cathodes for next-generation lithium-ion batteries (LIBs) with improved performance and stability.

2. Experimental

2.1 Materials

Nickel sulfate hexahydrate ($NiSO_4{\cdot}6H_2O$, 98.0% purity), cobalt sulfate heptahydrate ($CoSO_4{\cdot}7H_2O$, 99.5% purity), manganese sulfate monohydrate ($MnSO_4{\cdot}H_2O$, 99.9% purity), lithium hydroxide monohydrate ($LiOH{\cdot}H_2O$, 99.9% purity), sodium hydroxide (NaOH, 98.0% purity) and ammonium hydroxide solutions (28–30%, NH_4OH) were procured from VWR™ and used without further purification.

2.2 Synthesis of precursor

The $Ni_{0.8}Co_{0.1}Mn_{0.1}(OH)_2$ precursor cathode active materials (pCAM) were synthesized *via* a hydroxide co-precipitation method. Stoichiometric amounts of NiSO4·6H_2O, $CoSO_4{\cdot}7H_2O$, and $MnSO_4{\cdot}H_2O$, corresponding to a molar ratio of 0.8 : 0.1 : 0.1, were dissolved in deionized water to obtain a dark green solution with a concentration of 2.0 mol L^{-1}. The solution was then pumped into a 10 L stirred semi-batch reactor (SSBR) under a nitrogen atmosphere. Concurrently, 4.0 mol L^{-1} NaOH and 5.0 mol L^{-1} NH_4OH solutions were separately pumped into the reactor as a pH-regulating agent and a chelating agent, respectively. The stirring speed was maintained at 600 rpm and the pH of the reaction solution was controlled between 10.5–11.5 by adjusting the feed rate of the alkali solution. The reaction proceeded for 10 hours at a constant temperature of 50 °C. Subsequently, the precipitates were filtered, washed, and dried in a convection oven at 100 °C overnight. The resulting pristine $Ni_{0.8}Co_{0.1}Mn_{0.1}(OH)_2$ precursor powder was labeled as **p-NCM(OH)$_2$**. Further, the precursor was mixed with $LiOH{\cdot}H_2O$ at a molar ratio of 1 : 1.05. The mixture was calcined at 750 °C for 10 hours in an oxygen flow and then allowed to cool naturally to room temperature, yielding pristine $LiNi_{0.8}Co_{0.1}Mn_{0.1}O_2$ cathode material, designated as **p-LNCM**.

For the preparation of tungsten-doped pCAM, a specific amount of WO_3 was dissolved in 4.0 mol L^{-1} NaOH solution to form sodium tungstate (Na_2WO_4), which was continuously pumped into the SSBR under the same conditions as described for p-NCM$(OH)_2$ preparation. The tungsten-doped pCAM obtained through this wet process was denoted as **w-NCM(OH)$_2$**. After mixing with $LiOH{\cdot}H_2O$ at a molar ratio of 1 : 1.05 and further calcination at 750 °C for 10 hours in an oxygen flow, it was labeled as **w-LNCMW**.

For comparison, a tungsten-doped $LiNi_{0.8}Co_{0.1}Mn_{0.1}O_2$ cathode material was also prepared *via* a solid-state process. WO_3 powder, p-NCM$(OH)_2$, and $LiOH{\cdot}H_2O$ were mixed in an agate mortar and then calcined at 750 °C for 10 hours in an oxygen flow. Hereafter the synthesized W-doped $LiNi_{0.8}Co_{0.1}Mn_{0.1}O_2$ cathode material was designated as **s-LNCMW**.

2.3 Characterization

The powder samples were analyzed using a Rigaku MiniFlex 600 X-ray diffraction (XRD) instrument to acquire their XRD patterns. A six-multi-detector system was employed to collect XRD data at room temperature. Data was captured throughout two specific ranges, 10–80° 2θ, with a step width of 0.02°. For *ex situ* XRD measurements, the coin cells were disassembled in an Ar-filled glove box (Labmaster, MBRAUN Inc.). The cathodes were washed with DEC solvent, dried in an argon-filled controlled environment, and promptly transferred for XRD measurements. Rietveld refinement was conducted on XRD patterns using the Fullprof program to determine the lattice parameters of prepared samples. The morphologies and microstructures of the synthesized cathodes were examined using a ZEISS Crossbeam 540 scanning electron microscope (SEM) and transmission electron microscopy (TEM, 300 kV FE-TEM (Tecnai F-30 S-Twin)). The chemical compositions of the CAMs were analyzed using inductively coupled plasma optical emission spectroscopy (ICP-OES) by Thermo Fisher Scientific iCAP 6300 DUO instrument. The specific surface area of the CAM powders was measured *via* the multipoint Brunauer–Emmett–Teller (BET) experiments with N_2 adsorption and desorption isotherms using Belsorp Mini II. The tapped density value of CAMs was determined by using a BeDensi T1 instrument in accordance with the ASTM B527-20 standard, with a 50 g sample poured into the cylinder. The oxidation state and bonding information of the materials were determined using a NEXSA X-ray Photoelectron Spectrometer (XPS) from Thermo Scientific. The particle size distribution (PSD) was assessed using a Mastersizer 3000 (Malvern Panalytical).

2.4 Electrochemical measurement

The NCM composite slurries were composed of 90 wt% cathode active material, 4.5 wt% polyvinylidene fluoride

(PVDF) binder (Arkema HSV900), and 5.5 wt% conductive carbon black (Super P and KS-6, TIMCAL Graphite) dissolved in *N*-methyl-2-pyrrolidone (NMP, Sigma-Aldrich). The mixing process was carried out using a planetary mixer (ARV 310 Thinky) at 1200 rpm for 20 minutes. The resulting slurry was applied to an aluminum foil current collector using a doctor blade film applicator. It was then dried at 60 °C for 4 hours in a vacuum oven to ensure complete solvent removal. The cathode active material loading level and electrode density parameters were adjusted to 7.0 mg cm^{-2} and 3.2 g cc^{-1}, respectively.

The electrochemical performance of the NCM electrodes was tested by assembling CR2032-type coin half-cells in an Ar-filled glove box. The counter electrode was composed of lithium metal (AME-Energy). A polyolefin separator (Celgard 2320, 20 μm thick) was placed between negative and positive electrodes. The electrolyte consisted of a 1.2 M of $LiPF_6$ dissolved in a mixture of ethylene carbonate (EC) and ethyl methyl carbonate (EMC) in a 3 : 7 volume ratio, with an additional 2 wt% vinylene carbonate (VC). The cells underwent charging and discharging cycles at 30 °C, with a voltage range from 2.7 to 4.3 V. The process was carried out at a constant current density of 180 mA h g^{-1} (0.1C rate) using a Neware battery testing system MHW25 equipped with a constant-temperature chamber. All potentials were referenced to the lithium metal electrode.

2.5 Interfacial kinetics analysis

The interfacial behavior of cathode materials was investigated using a microcavity electrode. The cavity trap was filled by pressing the μ-cavity electrode against the as-prepared NCM composite slurry. The microelectrodes were then dried under vacuum at 90 °C overnight and subsequently were transferred into an Ar-filled glove box for electrochemical testing. A piece of Li metal and 1 M of $LiClO_4$ in a mixture of EC : PC (1 : 1 vol) were used as the counter electrode and electrolyte, respectively. The microelectrodes with NCM particles were charged and discharged for three cycles at 2 nA within a cut-off voltage range of 3.0–4.3 V using a galvanostat (IviumState model, Ivium). In a subsequent cycle, the microelectrode was fully recharged at 2 nA. However, positive and negative pulsed currents (pulse polarization process) were applied during discharging at certain depths of discharge (DOD). The pulsed currents were applied in the range of 2–80 nA. Tafel plots were generated using logarithmic pulsed currents and their potential responses to estimate kinetic parameters including exchange current density (i_0), charge transfer resistance (R_{ct}), and diffusion coefficient (D_{Li^+}). Detailed information about the preparation of microcavity electrodes and the pulse polarization process can be found in our published studies.[14,15]

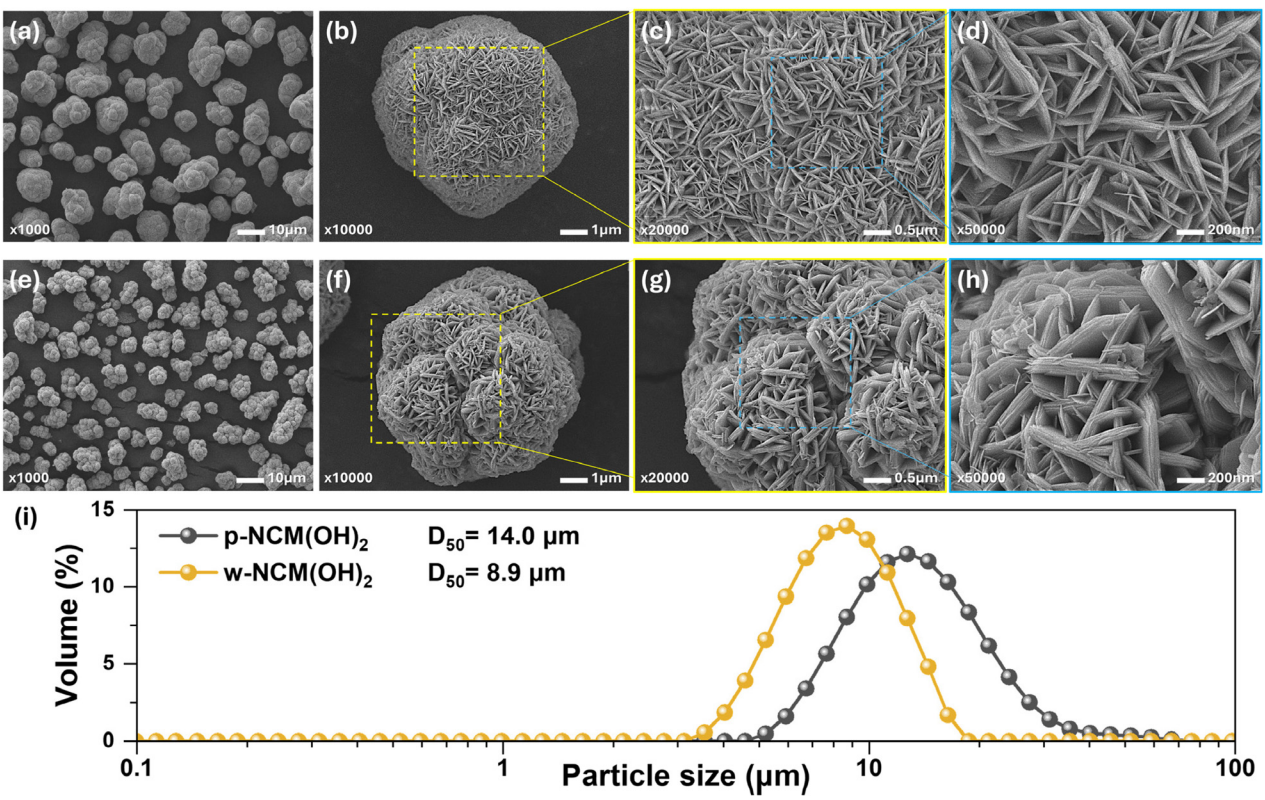

Fig. 1 SEM images of (a–d) p-NCM(OH) $_2$ and (e–h) w-NCM(OH)$_2$ precursors at various magnifications, along with the corresponding (i) particle size distribution analysis.

3. Results and discussion

Precise control and fine-tuning of synthesis parameters are critical to achieving desired outcomes in the performance of Ni-rich cathodes. Key parameters include the co-precipitation reaction temperature, stirring speed, system pH level, calcination temperature of the cathode materials, and the quality of raw materials. Meticulous manipulation of these factors is essential to ensure the optimal characteristics of the resulting material, making their careful optimization imperative for producing high-performance cathode materials.[16] Therefore, it is important to emphasize that all pCAM samples were synthesized using identical parameters for co-precipitation, calcination, and cell assembly to ensure credibility and reliability in assessing the influence of bulk and surface W-doping.

3.1. Morphology analysis

The SEM analysis was conducted to investigate the morphological properties of the pristine p-NCM$(OH)_2$ and W-doped w-NCM$(OH)_2$ precursors, obtained through the co-precipitation technique, as depicted in Fig. 1. Low-magnification images reveal that both p-NCM$(OH)_2$ (Fig. 1a and b) and w-NCM$(OH)_2$ (Fig. 1e and f) form spherical secondary particles at the micron scale. The average secondary particle diameter (D_{50}) values, shown in Fig. 1i, are 14.0 μm for the pristine precursor and 8.9 μm for the W-doped precursor. High-magnification images in Fig. 1d indicate that the pristine precursor p-NCM$(OH)_2$ consists of secondary particles formed from primary grains approx. 50 nm thick. In contrast, Fig. 1h demonstrates that the tungsten-doped w-NCM$(OH)_2$ secondary particles are formed from primary grains approx. 100 nm thick. These observations suggest that tungsten doping leads to a significant increase in the thickness of the primary grains and a reduction in the size of the secondary particles. Tungsten ions (W^{6+}) have a larger ionic radius (0.60 Å) compared to Ni^{3+} (0.56 Å), Co^{3+} (0.54 Å), and Mn^{4+} (0.53 Å). When incorporated into the precursor lattice, they can distort the crystal lattice, creating local strain. This strain can alter the energy barriers for nucleation and growth, promoting anisotropic growth of primary grains, leading to thicker grains. Additionally, tungsten ions may act as inhibitors to secondary particle agglomeration by increasing repulsive forces between primary grains, resulting in smaller secondary particles. The influence of these morphological changes on the electrochemical properties of the CAMs should be investigated to determine their impact on performance.

Fig. 2a, d and g present the SEM images depicting the typical morphologies of p-LNCM, w-LNCMW, and s-LNCMW cathode particles, respectively. All three CAMs were synthesized under identical two-step co-precipitation and calcination conditions, differing only in the W-dopant introduction route. According to SEM and PSD analysis, this synthesis resulted in spherical particles with an average diameter of approximately 10–13 μm as shown in Fig. 2j. The magnified images in Fig. 2b, e and h reveal that each secondary particle is composed of densely packed smaller primary particles. Despite the variations in doping routes and sample compositions, the size of these primary particles remains fairly consistent. Although previous studies have reported significant effects of dopants on primary particle size and shape,[17] we suggest that the absence of observed differences in our study may be due to the relatively low concentration of W-dopant employed (0.3 mol%). It is noteworthy that while the W-doped precursor w-NCM$(OH)_2$ showed the formation of thicker primary particles compared to the pristine p-NCM$(OH)_2$, the thickness of these primary particles remained unchanged during the subsequent calcination step, as demonstrated in ESI Fig. S1.† In contrast, the pristine precursor, which initially exhibited thinner primary particle architecture, experienced significant thickening during the calcination process. Comparable changes after calcination were observed for the surface-route W-doped s-LNCMW sample.

The chemical composition of the synthesized pCAMs and CAMs was determined using ICP-OES, as summarized in Table 1. The quantitative elemental analysis data from ICP closely matched the targeted 8 : 1 : 1 stoichiometric ratio, verifying that the compositions of the synthesized cathodes adhered to the intended NCM811 specifications. For both the surface and bulk tungsten (W) doping processes, the Li$[Ni_{0.8}Co_{0.097}Mn_{0.1}W_{0.003}]O_2$ cathode material was intentionally designed with W content of approximately 0.3 mol% or 0.56 wt%, which conforms to the planned formulation.

3.2. Structural analysis

X-ray diffraction (XRD) patterns were acquired to perform a comprehensive structural study of as-coprecipitated pristine and W-doped hydroxide precursors. As seen in Fig. 3a, both samples can be indexed as a typical fingerprint of a hexagonal phase β-Ni$(OH)_2$ with $P\bar{3}m1$ space group. The absence of any detectable impurities in the XRD patterns suggests that Co^{2+} and Mn^{2+} successfully substituted Ni^{2+} in the Ni$(OH)_2$ structure. The pronounced peaks at 2θ values of 19.18°, 33.06°, and 38.44° indicate exceptional crystallinity in both pristine and W-doped precursors.[18] The observed increase in the intensity ratio of the three main characteristic peaks for W-doped NCM$(OH)_2$ compared to the pristine NCM$(OH)_2$ indicates a notable change in the crystalline structure upon tungsten doping. More importantly, the increased values of the ratios I_{001}/I_{100} and I_{001}/I_{101} for the W-doped NCM$(OH)_2$, compared to the pristine sample, provide crucial insights into the preferential growth orientations of the primary particles or grains in these materials. These ratios suggest that the introduction of tungsten influences the crystal growth behavior, potentially altering the balance between the (001) and (100) planes. Typically, the primary particles of a hydroxide precursor exhibit a hexagonal-shaped lamellar crystal structure, with the (001) face predominantly exposed. This exposure can lead to the assembly of secondary particles where the (001) face is parallel to the radial direction and the (100) face is aligned with the circumference, assuming optimal precipitation conditions. The larger values of I_{001}/I_{100} and I_{001}/I_{101} in the W-doped sample imply a possible modification in this growth pattern, which may be due to

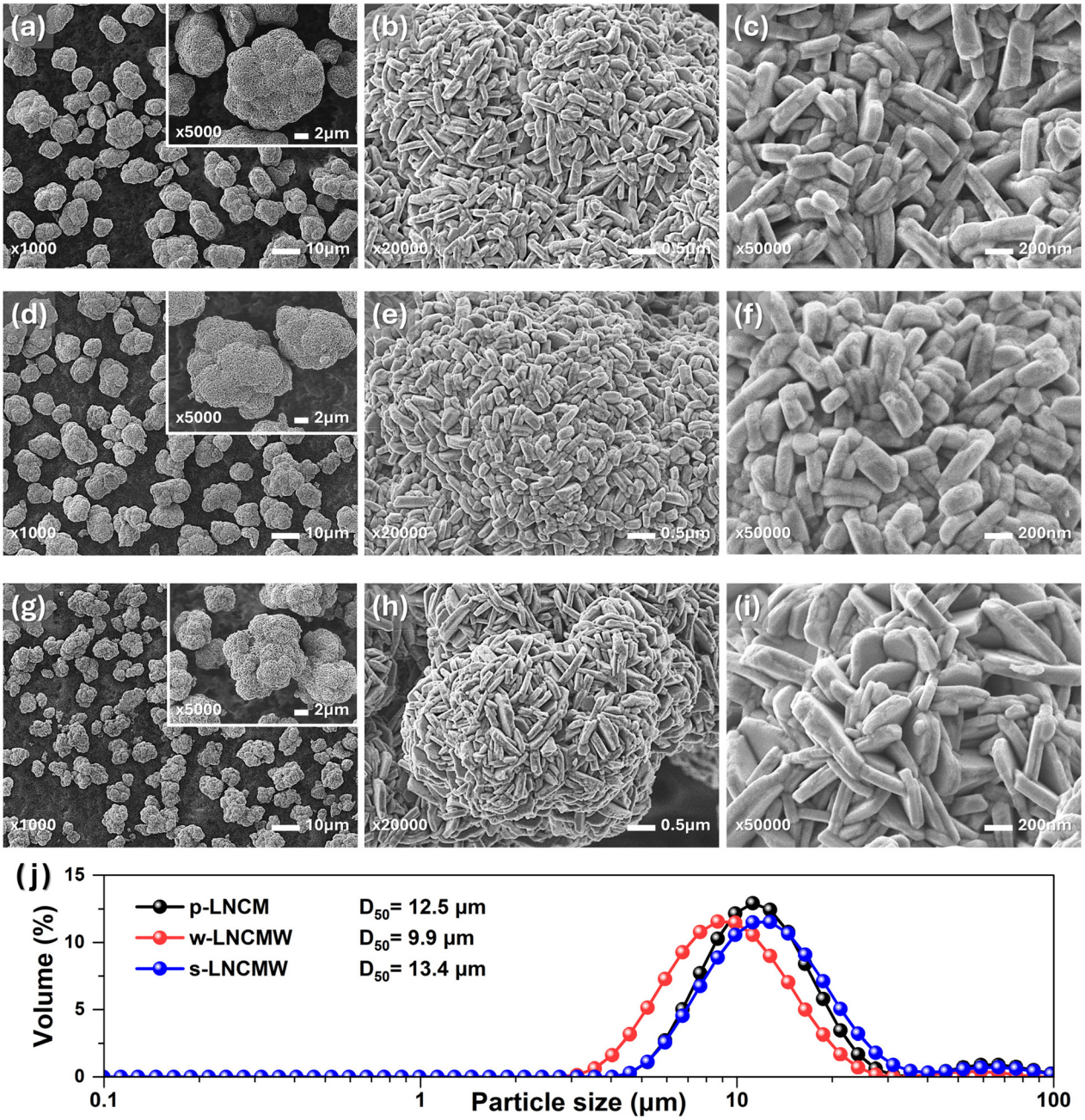

Fig. 2 SEM images of (a–c) p-LNCM, (d–f) w-LNCMW and (g–i) s-LNCMW cathode materials at various magnifications, along with the corresponding (j) particle size distribution analysis.

Table 1 ICP-OES results of obtained pCAMs and CAMs

	Mol (%)			
Sample	Ni	Co	Mn	Dopant (W)
p-NCM$(OH)_2$	79.79	10.15	10.06	—
w-NCM$(OH)_2$	79.72	9.98	9.99	0.31
p-LNCM	80.20	10.00	9.80	—
w-LNCMW	79.20	9.88	10.02	0.29
s-LNCMW	80.14	9.78	9.76	0.32

the impact of tungsten on the surface energy of these crystallographic planes. This modification could result in a more pronounced growth along the (001) direction, potentially leading to primary particles with enhanced alignment in the secondary particles, which is often associated with better electrochemical performance, as it can lead to more stable and efficient pathways for lithium-ion diffusion.[19] Such changes in the microstructure could have significant implications for the electrochemical properties of the material, particularly in terms of capacity, stability, and rate performance in LIBs.[20]

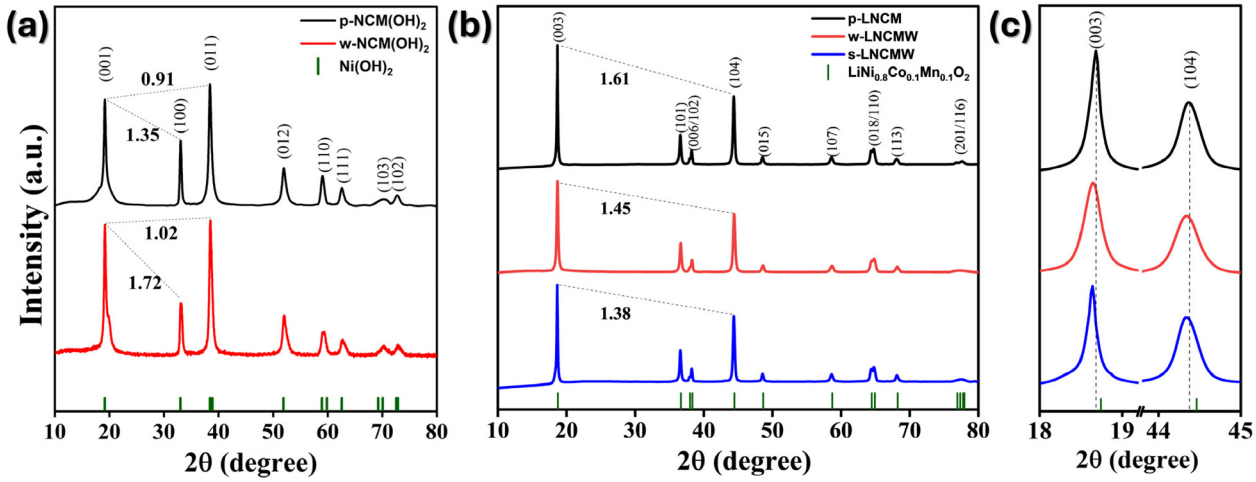

Fig. 3 XRD patterns of (a) pCAMs, (b) CAMs and (c) magnified view of (003) and (104) peaks.

The XRD patterns of both pristine and W-doped CAMs, as presented in Fig. 3b, exhibit a clear hexagonal α-$NaFeO_2$ structure with an $R\bar{3}m$ space group. This observation is consistent across all three samples, with no evidence of impurity phases detected. The high crystallinity of CAMs is demonstrated by the distinct peak splitting of the (108)/(110) reflections, as shown in Fig. 3b.[12] It is widely reported that the (003)/(104) peak intensity ratio serves as a reliable indicator of cation mixing level in layered CAMs, with values of 1.2 and above typically denoting a structurally ordered state.[4,12,22] In this study, the undoped p-LNCM sample exhibits a ratio of 1.61, indicative of its highly ordered structure and minimal cation mixing. With the introduction of W dopant, this ratio decreases to 1.45 in w-LNCMW and further to 1.38 in s-LNCMW. While this reduction suggests a reasonable increase in cation mixing, it is important to note that the ratios remain well above the critical threshold, affirming the structural integrity of the doped samples. As illustrated in Fig. 4, the Rietveld refinement process was conducted using an initial structural model of R-3m symmetry, with atomic positions, lattice parameters, and isotropic thermal factors derived from literature. The background was modeled using a Chebyshev polynomial, and peak shapes were fitted with a pseudo-Voigt function to accurately represent the diffraction data. Site occupancies of lithium and nickel were refined iteratively, with constraints applied to assess the degree of Li^+/Ni^{2+} mixing, a key parameter affecting electrochemical performance. The lattice parameters and unit cell volumes were refined to capture structural changes induced by tungsten doping, with variations consistent with the ionic radius of W^{6+}.

The introduction of W^{6+} ions into the TM sites necessitates the generation of Ni^{2+} ions to maintain charge balance. The increased presence of Ni^{2+} ions likely facilitates their migration into the Li layer due to the comparable ionic radii of Ni^{2+} and Li^+ (rNi^{2+} = 0.69 Å, rLi^+ = 0.72 Å, rCo^{3+} = 0.55 Å, rMn^{4+} = 0.53 Å, rNi^{3+} = 0.56 Å and rW^{6+} = 0.60 Å). Moreover, the substitution of Ni^{3+} by the larger Ni^{2+} ions in the TM sites is expected to result in an expansion of the unit cell volume. This hypothesis is confirmed by the unit cell volume calculations based on the refined lattice parameters in Table 2, which show increase in cell volume in W-doped samples, consistent with previous observations in W-doped $LiNiO_2$[21] and NCM[10] cathodes. In addition, despite modest variations in the c/a ratios among the different samples, all of them were over 4.9, which indicates

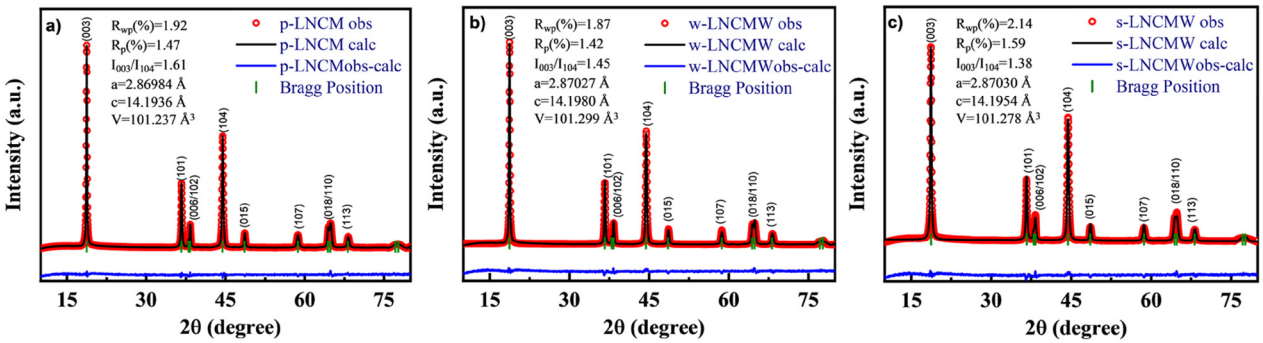

Fig. 4 XRD Rietveld refinement profiles of (a) p-LNCM; (b) w-LNCMW; (c) s-LNCMW.

Table 2 The calculated lattice parameters of the corresponding CAMs

Sample	a (Å)	c (Å)	V (Å)	c/a	I_{003}/I_{104}	R_{wp}, %
p-LNCM	2.86984	14.1936	101.237	4.9457	1.61	1.92
w-LNCMW	2.87027	14.1980	101.299	4.9465	1.45	1.87
s-LNCMW	2.87030	14.1954	101.278	4.9449	1.38	2.14

that all three samples had excellent crystallinity and a layered structure.[22]

It is important to highlight that the magnified view of the (003) and (104) peaks in Fig. 3c reveals a leftward shift, further corroborating our hypothesis of W^{6+} species incorporation into the layered structure of NCM811, resulting in an increased interlayer distance between the lattices. This structural modification has the potential to create broader pathways for lithium-ion transport within the W-doped CAMs, thereby facilitating more efficient diffusion of lithium ions.[23]

The BET analysis reveals that the wet-route W-doped w-LNCMW exhibits a higher specific surface area (SSA) and larger pore size compared to both pristine NCM and solid-route W-doped s-LNCMW (Table 3). This higher SSA is indicative of a more extensive surface area, which is likely due to the finer particle size distribution observed in the w-LNCMW material (Fig. 2j). The D_{50} value of 9.9 μm, as obtained from PSD analysis, supports this finding, suggesting that the W-doping by wet-processing method results in smaller secondary particles, thereby enhancing the material's overall surface area. Furthermore, the tap density measurements indicate a slight decrease in density for the w-LNCMW sample compared to the pristine p-LNCM, which may be attributed to the finer particle structure of the wet-processed material. This interplay between SSA, pore size, and tap density is critical for optimizing the performance of NCM cathodes, particularly in terms of their electrochemical properties and overall energy storage capabilities.[24,25]

To confirm the rearrangement of the surface structure, Fig. S3† presents TEM, HR-TEM, and SAED images of the p-LNCM particle. Fig. S3(a, b, d and e)† demonstrate that the p-LNCM cathode features a smooth surface. The HR-TEM images indicate surface layer spacings of 4.71 Å for the d(003) plane and 3.4 Å for the d(101) plane. The SAED pattern shows distinct and high-quality diffraction spots, suggesting that the NCM sample exhibits good crystallization.

The HRTEM image (Fig. S4†) showcases the lateral facet (highlighted in the green box in Fig. S4d†) with clear lattice fringes.[26] The measured spacing is 4.93 Å, which is closely aligned with the distance between lithium-ion layers in the crystal structure. Furthermore, the light blue dotted lines indicate a break in the lattice fringes, resulting in an interplanar spacing of 2.337 Å, which is half of the original spacing.

The lateral cross-sectional view of the crystal structure's (010) facet illustrates this configuration. The hexagonal plate-like single crystal precursors present frontal crystal facets on the top and bottom (denoted as {001}), along with six similar prismatic lateral facets from the (010) group.[27] In these precursors' β-Ni(OH)2 crystal structure, each (001) facet layer consists of closely packed TM(OH)6 octahedra that share corner oxygen atoms. The topmost hydroxyl group of the $TM(OH)_6$ octahedron is exposed on the (001) facet, creating a dense network of hydrogen bonds. Although the (010) facet of the precursors is also accessible to hydroxyl groups, it additionally contains coordinatively unsaturated transition metal sites.

XPS spectra (Fig. 5) provide key insights into the oxidation states and surface compositions of the pristine and W-doped NCM cathode materials. The Ni 2p spectra for all samples show two primary peaks corresponding to Ni $2p_{3/2}$ and Ni $2p_{1/2}$, located at binding energies of approximately 853.91 eV and 872.35 eV for the pristine sample (p-LNCM), and slightly shifted for the W-doped samples (s-LNCMW and w-LNCMW). These shifts suggest alterations in the local electronic environment due to W doping. It is noteworthy that the Ni^{3+} peaks are more pronounced in both doped samples compared to the pristine material. Additionally, intense Ni^{2+} peaks can be observed, as doping with high-valent ions, such as W^{6+}, can lead to an increased proportion of Ni^{2+} to maintain charge neutrality. This change enhances the cyclic stability of nickel-rich materials, contributing to improved structural stability and electrochemical performance of lithium-ion batteries (LIBs). The Mn 2p spectra confirm the presence of Mn^{4+}, with peaks for Mn $2p_{3/2}$ observed at 641.94 eV (p-LNCM), 641.16 eV (s-LNCMW), and 641.28 eV (w-LNCMW). The relatively consistent positions of these peaks across the samples indicate that the Mn oxidation state remains largely unaffected by W doping. Similarly, the Co 2p spectra exhibit two distinct peaks for Co $2p_{3/2}$ and Co $2p_{1/2}$, confirming the Co^{3+} oxidation state in all samples. The slight shifts in the binding energies of Co peaks in W-doped samples suggest some degree of interaction between Co and W at the surface level. The W 4f spectra reveal the successful incorporation of W^{6+} into both the w-LNCMW and s-LNCMW samples, with W $4f_{7/2}$ and W $4f_{5/2}$ peaks observed at approximately 36.70 eV and 34.80 eV, respectively. The presence of these peaks confirms the W doping in the lattice, where W^{6+} ions likely occupy transition metal (TM) sites, contributing to the stabilization of the NCM structure and enhancing the electrochemical properties of the material. Overall, the XPS results indicate that W doping modifies the surface chemical states of Ni, Co, and Mn in the NCM cathode materials. This alteration, particularly the enhanced Ni^{3+} content, likely contributes to the improved cycling stability and electrochemical performance observed in the W-doped samples. Moreover, the incorporation of W^{6+} ions at the surface helps to reduce unwanted side reactions at the elec-

Table 3 The surface area and tap density values of CAMs

Samples	SSA ($m^2\ g^{-1}$)	Pore size (nm)	Tap density ($g\ cm^{-3}$)
p-LNCM	0.29	8.14	2.15
w-LNCMW	0.47	10.16	2.02
s-LNCMW	0.31	7.61	2.25

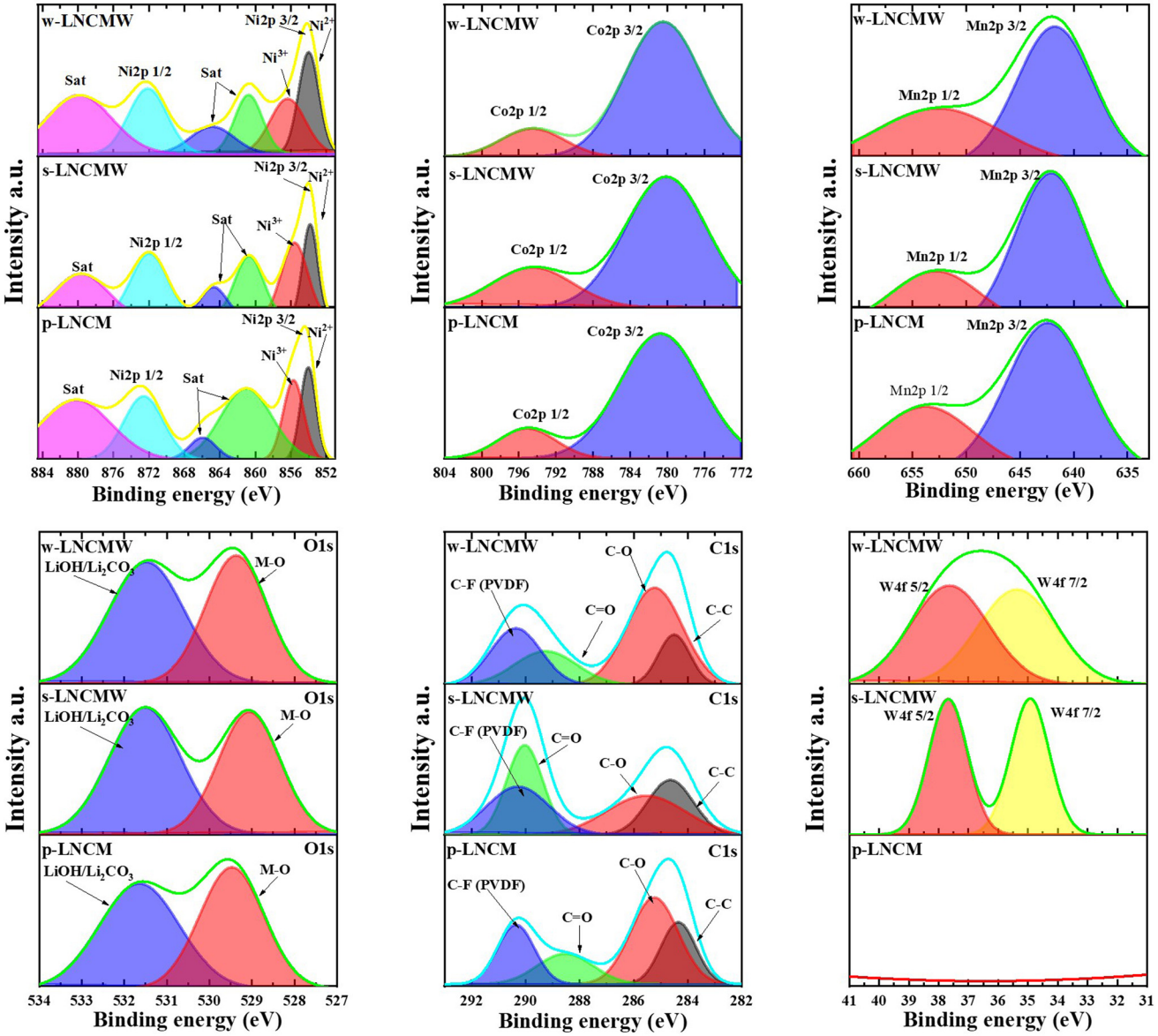

Fig. 5 High-resolution XPS spectra of Ni 2p, Co 2p, Mn 2p, O 1s, C 1s and W 4f of p-LNCM, w-LNCMW and s-LNCMW cathode materials.

trode–electrolyte interface, further stabilizing the material during prolonged cycling.

Raman spectroscopy was utilized to characterize the synthesized samples' particular structure, surface state, and composition. This approach is generally used as a surface probe study, sensitive to the short-range environment of oxygen coordination around cations in oxide frameworks.[28] Fig. 6 shows the Raman spectrum of pristine NCM811 (black line), revealing three prominent bands at 301, 432, and 833 cm^{-1}. These bands correspond to active modes of the layered $LiMO_2$ (M = Ni, Mn, or Co) lattice (D_3d^5 spectroscopic symmetry). This vibrational pattern indicates the excellent crystallinity and rhombohedral crystal structure of p-LNCM, which is consistent with the XRD data.[29,30] The irreducible representation was used to identify the Raman-active vibrational modes of layered $LiMO_2$ (M = Ni, Mn, or Co) compounds. The vibrational modes of each transition-metal ion are given as $\Gamma = 2A_{2u} + 2E_{2u} + A_{1g} + E_g$, where only A_{1g} and E_g are Raman active.[31,32] These come from the M–O stretching and O–M–O bending modes, respectively. $LiNi_{0.8}Co_{0.1}Mn_{0.1}O_2$ has three distinct transition-metal cations (M = Ni + Mn + Co) in the Wyckoff site of the rhombohedral structure, allowing for spectrum deconvolution utilizing three pairs (A_{1g} + E_g) of Raman modes.[33] The s-LNCMW's Raman spectra show additional three distinct bands at 1562, 1726, and 2869 cm^{-1}, distinguishing it from pristine material. This demonstrates significant structural changes in the surface vibrational modes of W-doped crystals. The s-LNCMW Raman spectrum shows three: (a) the fundamental modes of

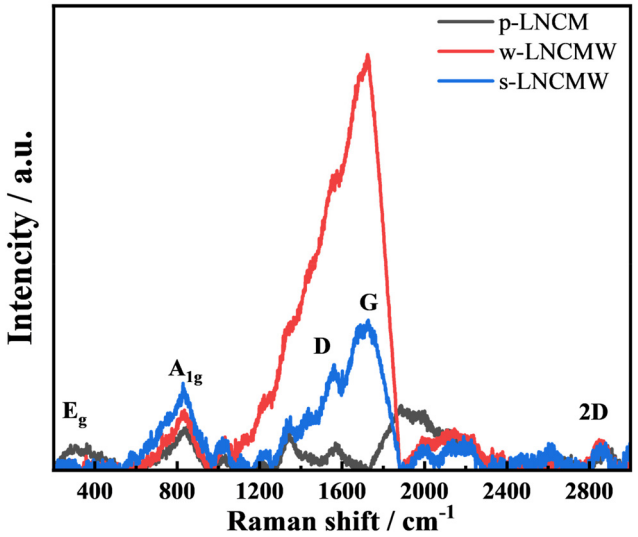

Fig. 6 The Raman spectra of the cathode active materials.

the NCM811 lattice with a characteristic peak at 1562 cm^{-1} (O–Ni–O bonds) of the D_3d^5 spectroscopic symmetry and (b) a strong band at 1726 cm^{-1} corresponding to the presence of W–O.[34] The w-LNCMW Raman spectra show an intense peak at 1725 cm^{-1} and a possible explanation for the widening of Raman bands for Ni-containing compounds is the Ni/Li cation mixing (Ni on Li site), which confirms the XRD results of a greater Ni/Li cationic disorder in the doped sample.

3.2 Electrochemical performance

The electrochemical performance of the p-LNCM, w-LNCMW, and s-LNCMW cathodes was systematically investigated using 2032 coin-type half cells, paired with a lithium metal anode. The CAMs underwent an initial formation cycling process at 0.1C (where 1C corresponds to 180 mA g^{-1}) for three cycles, followed by cycling at 0.2C within a voltage window of 2.7 V to 4.3 V. The resulting charge–discharge profiles, which are characteristic of high-nickel cathode active materials, are presented in Fig. 7a–c.

The undoped p-LNCM cathode exhibited an initial discharge capacity of 193 mA h g^{-1}, similar to the tungsten-doped w-LNCMW and s-LNCMW samples, which demonstrated initial discharge capacities of 201 mA h g^{-1} and 198 mA h g^{-1}, respectively. The reduced discharge capacity of the p-LNCM cathode can be attributed to microcrack formation at the initial delithiation process, which increases the exposed surface area and leads to extensive SEI formation. This phenomenon results in the consumption of active lithium and degradation of the cathode's electrochemical performance, as previously reported.[35] Moreover, the pristine p-LNCM cathode displayed a significant increase in polarization during discharge by the 200th cycle, which was accompanied by a sharp decline in capacity. The capacity retention dropped to 75%, at which point the cycling test was terminated. This suggests that the undoped material suffers from severe structural degradation and impedance growth over prolonged cycling, limiting its practical application in EVs. The enhancement in initial capacity for the doped materials suggests that tungsten doping effectively increases the lithium-ion storage capability, potentially through the stabilization of the crystal structure *via* W–O bonding. The presence of W–O bonds could contribute to a more robust lattice framework, reducing structural degradation during cycling and facilitating the intercalation and deintercalation of lithium ions. This structural stabilization is likely a key factor in the observed improvement in both initial capacity and cycling stability of the tungsten-doped cathodes.

In contrast, the tungsten-doped cathodes exhibited markedly superior cycling stability. The s-LNCMW cathode, in particular, demonstrated outstanding long-term performance, retaining 92% of its initial capacity after 500 cycles. The w-LNCMW cathode also showed considerable stability, maintaining 85% of its initial capacity after 385 cycles. These results suggest that tungsten doping not only enhances the initial electrochemical performance but also significantly improves the structural integrity of the material during extended cycling. The superior performance of s-LNCMW compared to w-LNCMW can be attributed to differences in the distribution or incorporation of tungsten within the lattice and partial surface coating by protective Li_xWO_y layer.

The Fig. 8 illustrates the rate capability of undoped (p-LNCM), bulk tungsten-doped (w-LNCMW), and surface tungsten-doped (s-LNCMW) NCM samples. The voltage *vs.* specific capacity curves (a–c) show the discharge behavior at various C-rates (0.1C, 0.2C, 0.5C, 1C, and 2C). The pristine p-LNCM sample exhibits lower capacities across all C-rates compared to both W-doped samples. The bulk-doped w-LNCMW shows moderate performance, improving upon the undoped sample but falling short of the surface-doped s-LNCMW. The s-LNCMW sample demonstrates superior specific capacity retention and lower polarization, indicating enhanced rate capability. Fig. 8d depicts the cycling stability and rate performance of the three samples. Notably, the capacity retention of s-LNCMW remains stable upon returning to 0.1C after cycling at elevated rates, suggesting minimal structural degradation and superior electrochemical stability. The improved performance of s-LNCMW can be attributed to the surface doping strategy and partial surface coating by a protective Li_xWO_y layer, which likely mitigates surface-side reactions and structural deterioration while enhancing ionic conductivity at the electrode–electrolyte interface. In contrast, the bulk doping of w-LNCMW, although beneficial, does not provide the same degree of surface stability and kinetic enhancement as s-LNCMW. This study highlights the potential of surface tungsten doping, combined with the formation of a protective Li_xWO_y coating layer, as a viable approach to boost the high-rate performance and cycling stability of NCM cathode materials for lithium-ion batteries.

The Nyquist plot presented in the Fig. 8e compares the potentiostatic electrochemical impedance spectra (PEIS) of undoped (p-LNCM), bulk tungsten-doped (w-LNCMW), and

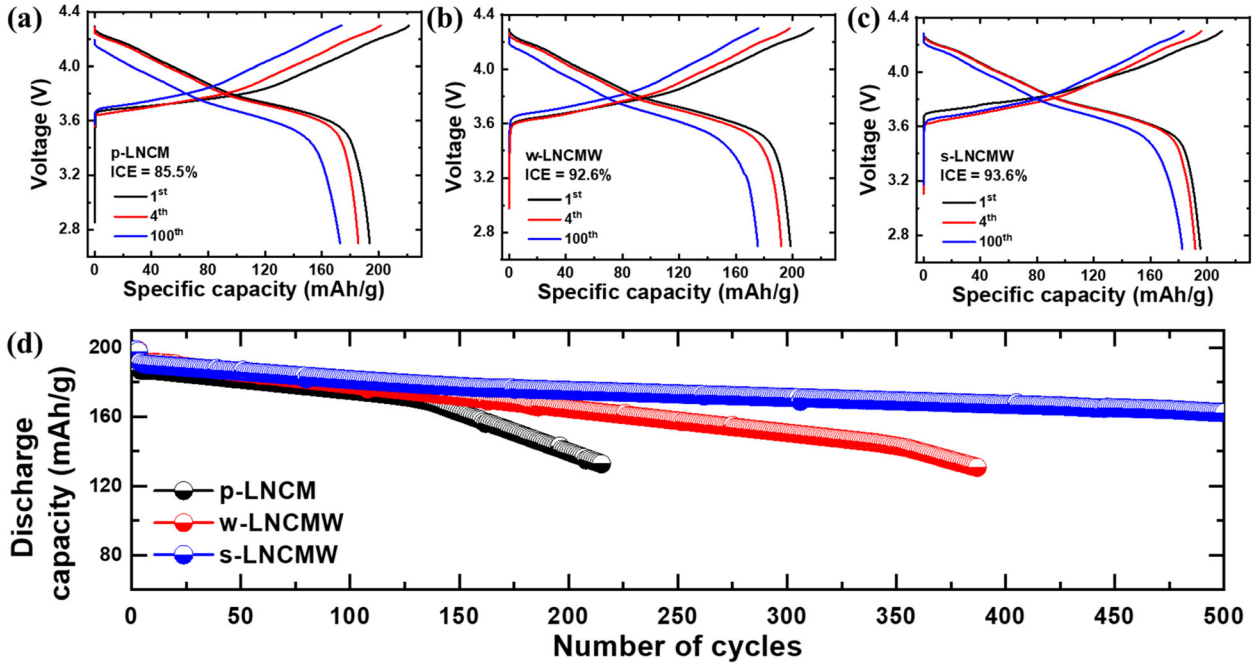

Fig. 7 Galvanostatic charge–discharge voltage profiles of (a) p-LNCM, (b) w-LNCMW and (c) s-LNCMW cathode materials. (d) Cycle performance of CAMs at 0.1C for 3 cycles and at 0.2C for subsequent cycles.

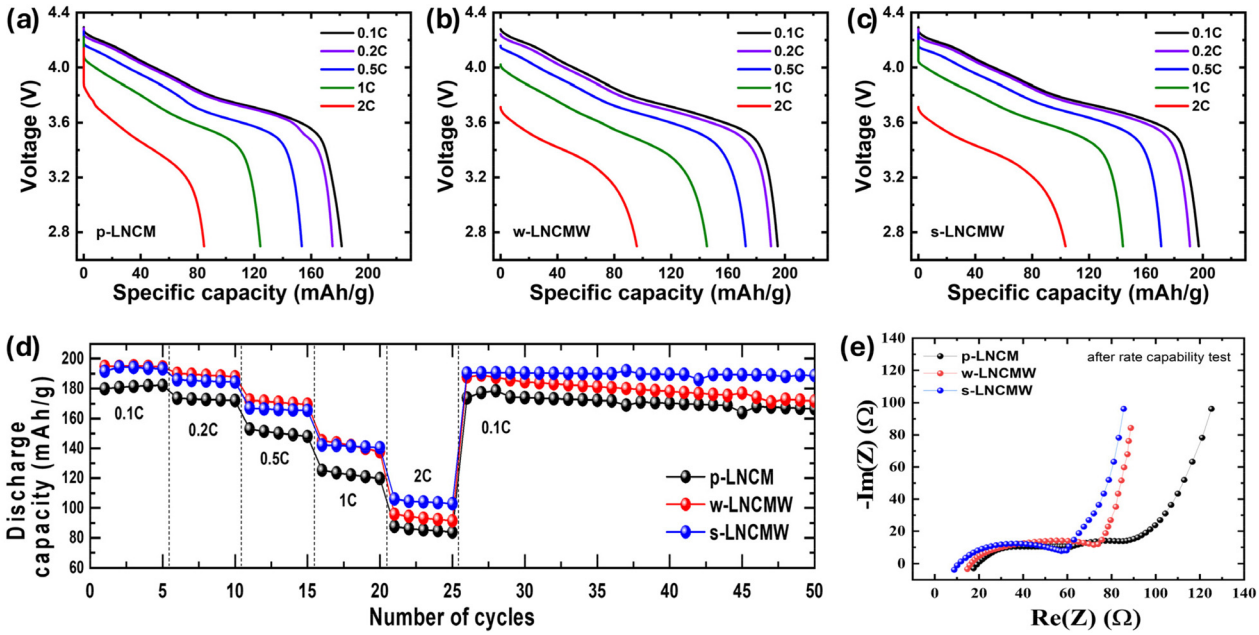

Fig. 8 Galvanostatic discharge voltage curves of (a) p-LNCM, (b) w-LNCMW and (c) s-LNCMW cathode materials at specified current densities. (d) Rate capability performance of CAMs at 0.1C, 0.2C, 0.5C, 1C and 2C for 5 cycles. (e) PEIS results presented as Nyquist plots for CAMs after rate capability test.

surface tungsten-doped (s-LNCMW) NCM samples after rate capability test. The plot illustrates the relationship between the real part (Re(Z)) and imaginary part (Im(Z)) of impedance, indicating the overall resistance and charge transfer kinetics within the electrode materials. The undoped p-LNCM sample exhibits the highest charge transfer resistance (R_{ct}), as evidenced by the larger diameter of the semicircle in the high-frequency region. This suggests sluggish charge transfer and limited electrochemical activity at the electrode–electrolyte interface. The bulk tungsten-doped w-LNCMW sample shows a

noticeable reduction in R_{ct} compared to the pristine material, reflecting the beneficial effects of tungsten incorporation in enhancing ionic and electronic conductivity. The s-LNCMW sample, however, outperforms both p-LNCM and w-LNCMW, displaying the smallest semicircle and the lowest R_{ct} among the three samples. This improved impedance profile can be attributed to the surface-specific tungsten doping, which likely facilitates faster charge transfer processes by forming a more conductive electrode surface and reducing the resistance at the interface. Furthermore, the partial coating of a Li_xWO_y layer on the surface of s-LNCMW may act as a protective barrier, minimizing undesirable side reactions and improving the overall structural stability of the electrode material. Overall, the EIS results demonstrate that the surface tungsten doping strategy effectively enhances the electrochemical kinetics of NCM cathode materials, making s-LNCMW a promising candidate for high-performance lithium-ion batteries.

A postmortem analysis was conducted to investigate potential degradative phenomena at the electrode level following high-rate performance evaluations and EIS analysis. This approach was aimed at correlating the structural integrity and electrochemical behavior of the electrodes under rigorous operational conditions. As illustrated in Fig. S2,† the cross-sectional morphology of all electrodes remained relatively stable, indicating the robustness of the electrode architecture against high-rate cycling. The absence of significant structural distortions, delamination, or active material detachment suggests that the binder and conductive matrix provided adequate mechanical support during prolonged electrochemical stress. Furthermore, the uniform thickness of the electrodes implies minimal mechanical compression or expansion effects, which are often observed in systems with poor electrode stability.

3.3 Interfacial kinetics analysis

A microcavity electrode measurement was conducted to demonstrate the impact of W-doping on the kinetics of the NCM cathode material. Fig. 9 shows the charge–discharge profiles of the cathode materials for the initial three cycles measured at 2 nA, which corresponds to a rate of approximately 0.3C. Each microelectrode, containing the respective cathode active material particles, delivered discharge capacities of ~5.6–5.8 nA h, with initial CEs of ~84–87%. The theoretical capacity for a single cathode particle was estimated based on the average particle sizes of the cathode materials, assuming an actual capacity of 200 mA h g^{-1} and a theoretical density of 4.85 g cm^{-3}.[36,37] Based on this estimation, approximately 4–5 cathode particles were expected to be present within each microelectrode hole.

All microelectrodes with cathode particles demonstrated reversible discharge capacities after three cycles. Based on the discharge capacities from the third cycle, the pulse polarization process was performed at specific depths of discharge (DOD) states, adjusted in 10% increments, in the subsequent cycle. Fig. S5a and b† show the applied pulsed currents and corresponding potential response curves at DOD 50%, along with Tafel plots, where the measured points were fitted by straight lines (anodic and cathodic Tafel slopes). The charge transfer coefficient (α) in the Tafel equation was theoretically assumed to be 0.5 for both the charge and discharge reactions of the cathode.[38]

Fig. 10 illustrates the Tafel plots of the cathode materials, generated using the logarithmic applied pulsed currents and overpotentials. As the current increases, a non-linear trend is observed in all Tafel plots for the cathode materials. Slight differences in overpotentials were noted between the p-LNCM and w-LNCMW cathodes across all DOD states. However, s-LNCMW showed significant improvement in the high current ranges compared to the other cathodes. This behavior is primarily attributed to differences in exchange current density and Li^+ diffusivity among the cathodes.[39] Additionally, all cathode materials exhibited higher overpotentials at the end of the discharge process due to the DOD-dependent kinetic limitations of NCM cathode materials.

According to the calculations, a considerably high i_0, especially at mid-DOD states, was observed for tungsten-doped CAMs compared to the pristine material as shown in Fig. 11. As expected, pristine cathode exhibited a higher R_{ct} (160–900 Ω cm^2), while the R_{ct} values of tungsten doped CAMs ranged from approximately 120–707 Ω cm^2 and 94–562 Ω cm^2 for bulk-doped and surface-doped cathodes, respectively. The results indicate that surface doping is more favorable, as the conductive protective layer helps minimize the interfacial resistance of NCM cathode particles. The diffusion coefficients of CAMs, calculated using Fick's law, further confirm that the doping strategy enhances Li-ion transport.

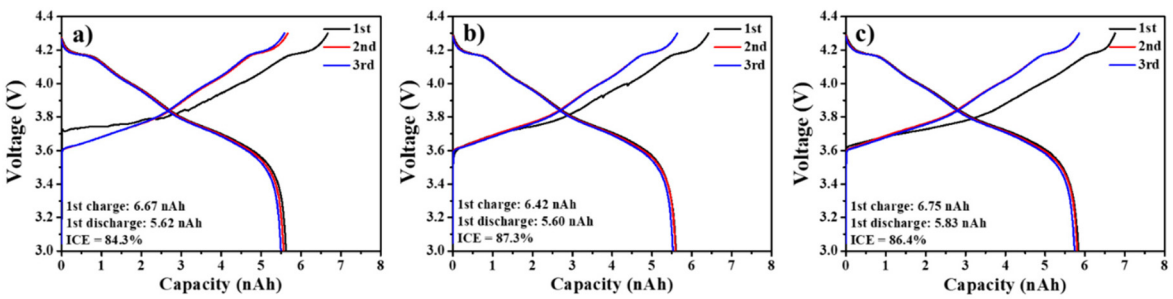

Fig. 9 Galvanostatic charge–discharge voltage profiles of (a) p-LNCM, (b) w-LNCMW, and (c) s-LNCMW cathode materials measured at 2 nA using a microcavity electrode.

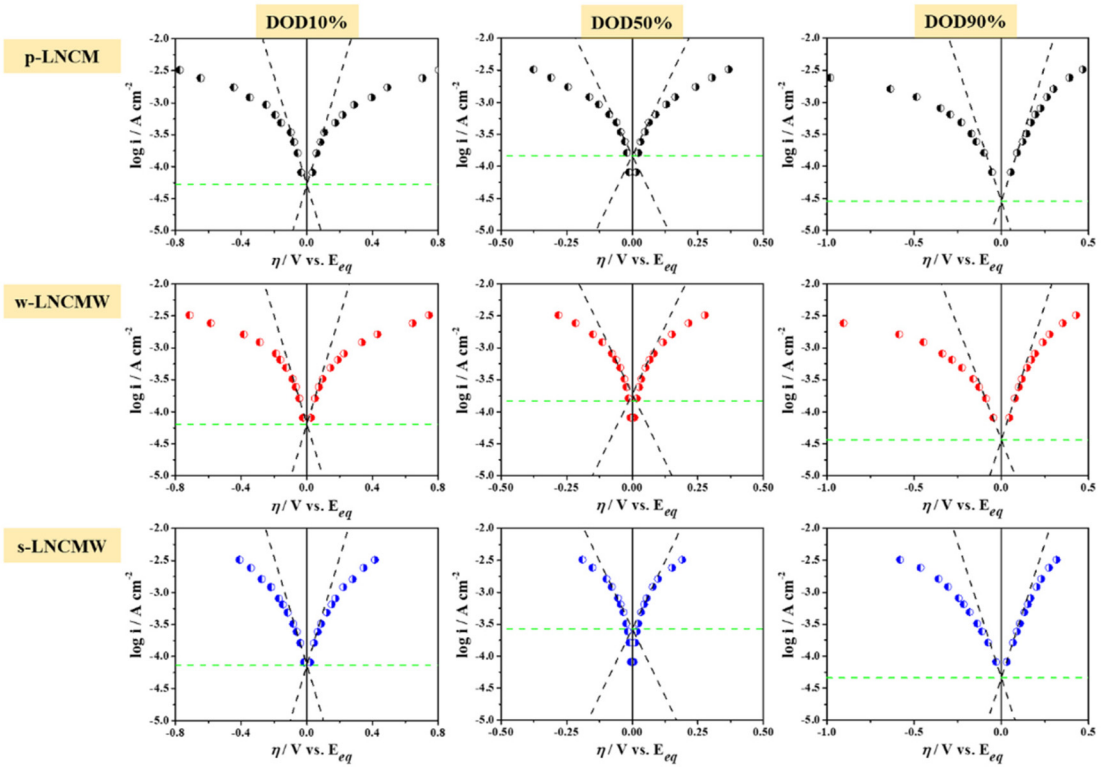

Fig. 10 Tafel plots of CAMs at DOD10%, DOD50%, and DOD90% states.

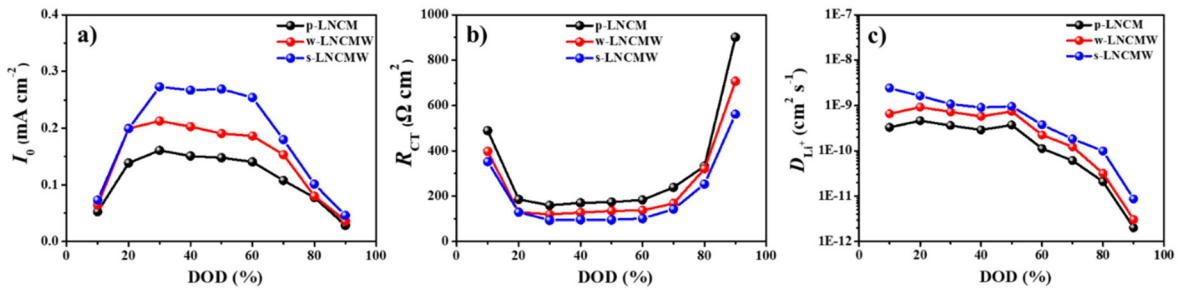

Fig. 11 The calculated kinetic parameters (a) exchange current density, (b) charge transfer resistance, and (c) Li^+ diffusion coefficient of the CAMs.

4. Conclusions

This study presents a comprehensive comparative analysis of W-doped high-nickel $LiNi_{0.8}Co_{0.1}Mn_{0.1}O_2$ (NCM811) cathode materials, synthesized through different methods. It focuses on their structural, morphological, and electrochemical performance. The findings reveal that surface W-doping significantly enhances electrochemical stability, rate capability, and overall cycling performance compared to bulk W-doping and undoped NCM811 cathodes.

The surface W-doped NCM811 (s-LNCMW) demonstrated an impressive capacity retention of 92% after 500 cycles, outperforming both the pristine and bulk W-doped counterparts. This superior performance is attributed to lower charge transfer resistance and improved structural stability afforded by the surface-specific W-doping. The inclusion of W^{6+} ions in the lattice contributes to structural stabilization by reducing cation mixing and facilitating lithium-ion diffusion. Additionally, the formation of a protective Li_xWO_y layer on the surface helps mitigate side reactions at the electrode–electrolyte interface, thereby reducing impedance growth and preserving the material's integrity during extensive cycling.

The bulk W-doped NCM811 (w-LNCMW) samples also showed notable improvements in initial discharge capacity and structural integrity compared to the undoped material, confirming that W-doping enhances the stability of the crystal lattice. However, surface W-doping proved to be a more effective strategy for reducing surface degradation, thereby improving the material's rate capability and long-term cycling stability.

The study concludes that surface W-doping, combined with a partial protective coating, represents a promising approach for optimizing high-nickel NCM cathodes in lithium-ion batteries, particularly for applications requiring high energy density and extended cycle life, such as electric vehicles and grid energy storage.

Data availability

The data supporting this article have been included in the ESI.†

Conflicts of interest

There are no conflicts to declare.

Acknowledgements

This research was funded by the Science Committee of the Ministry of Science and Higher Education of the Republic of Kazakhstan (Grant No. AP13068160). We also acknowledge support from the research grant 0122022FD4136 from Nazarbayev University, Program Targeted Funding BR21882402 and BR24992766 from the Ministry of Science and Higher Education of the Republic of Kazakhstan.

References

1 H. H. Ryu, K. J. Park, C. S. Yoon and Y. K. Sun, Capacity fading of Ni-rich $Li[Ni_xCo_yMn_{1-x-y}]O_2$ ($0.6 \leq x \leq 0.95$) Cathodes for High-Energy-Density Lithium-Ion Batteries: Bulk or Surface Degradation?, *Chem. Mater.*, 2018, **30**, 1155–1163, DOI: **10.1021/acs.chemmater.7b05269**.

2 S. T. Myung, F. Maglia, K. J. Park, C. S. Yoon, P. Lamp, S. J. Kim and Y. K. Sun, Nickel-Rich Layered Cathode Materials for Automotive Lithium-Ion Batteries: Achievements and Perspectives, *ACS Energy Lett.*, 2017, **2**, 196–223, DOI: **10.1021/acsenergylett.6b00594**.

3 J. H. Kim, K. J. Park, S. J. Kim, C. S. Yoon and Y. K. Sun, A method of increasing the energy density of layered Ni-rich Li[Ni 1-2: X Co x Mn x]O 2 cathodes (x = 0.05, 0.1, 0.2), *J. Mater. Chem. A*, 2019, 7, 2694–2701, DOI: **10.1039/c8ta10438g**.

4 L. Hou, Q. Liu, X. Chen, Q. Yang, D. Mu, L. Li, F. Wu and R. Chen, In-depth understanding of the deterioration mechanism and modification engineering of high energy density Ni-rich layered lithium transition-metal oxide cathode for lithium-ion batteries, *Chem. Eng. J.*, 2023, **465**, 142946, DOI: **10.1016/j.cej.2023.142946**.

5 M. Bianchini, M. Roca-Ayats, P. Hartmann, T. Brezesinski and J. Janek, There and Back Again—The Journey of $LiNiO_2$ as a Cathode Active Material, *Angew. Chem., Int. Ed.*, 2019, **58**, 10434–10458, DOI: **10.1002/anie.201812472**.

6 P. Mukherjee, P. Lu, N. Faenza, N. Pereira, G. Amatucci, G. Ceder and F. Cosandey, Atomic Structure of Surface-Densified Phases in Ni-Rich Layered Compounds, *ACS Appl. Mater. Interfaces*, 2021, **13**, 17478–17486, DOI: **10.1021/acsami.1c00143**.

7 J. Xu, E. Hu, D. Nordlund, A. Mehta, S. N. Ehrlich, X. Q. Yang and W. Tong, Understanding the degradation mechanism of lithium nickel oxide cathodes for Li-ion batteries, *ACS Appl. Mater. Interfaces*, 2016, **8**, 31677–31683, DOI: **10.1021/acsami.6b11111**.

8 C. S. Yoon, D. W. Jun, S. T. Myung and Y. K. Sun, Structural Stability of $LiNiO_2$ Cycled above 4.2 v, *ACS Energy Lett.*, 2017, **2**, 1150–1155, DOI: **10.1021/acsenergylett.7b00304**.

9 D. H. Kim, J. H. Song, C. H. Jung, D. Eum, B. Kim, S. H. Hong and K. Kang, Stepwise Dopant Selection Process for High-Nickel Layered Oxide Cathodes, *Adv. Energy Mater.*, 2022, **12**, 1–9, DOI: **10.1002/aenm.202200136**.

10 M. Dalkilic, A. Schmidt, T. D. Schladt, P. Axmann, M. Wohlfahrt-Mehrens and M. Lindén, W-Doping, of Dense NMC811 Hydroxide through Wet-Impregnation and Its Impact on Crystal Structure, Phase Transition Related Gas Evolution and Electrochemical Performance at Elevated Upper Cut-Off Voltage, *J. Electrochem. Soc.*, 2022, **169**, 120501, DOI: **10.1149/1945-7111/aca360**.

11 U. H. Kim, N. Y. Park, G. T. Park, H. Kim, C. S. Yoon and Y. K. Sun, High-Energy W-Doped $Li[Ni_{0.95}Co_{0.04}Al_{0.01}]O_2$ Cathodes for Next-Generation Electric Vehicles, *Energy Storage Mater.*, 2020, **33**, 399–407, DOI: **10.1016/j.ensm.2020.08.013**.

12 G. T. Park, H. H. Ryu, N. Y. Park, C. S. Yoon and Y. K. Sun, Tungsten doping for stabilization of $Li[Ni_{0.90}Co_{0.05}Mn_{0.05}]O_2$ cathode for Li-ion battery at high voltage, *J. Power Sources*, 2019, **442**, 227242, DOI: **10.1016/j.jpowsour.2019.227242**.

13 F. Reissig, M. A. Lange, L. Haneke, T. Placke, W. G. Zeier, M. Winter, R. Schmuch and A. Gomez-Martin, Synergistic Effects of Surface Coating and Bulk Doping in Ni-Rich Lithium Nickel Cobalt Manganese Oxide Cathode Materials for High-Energy Lithium Ion Batteries, *ChemSusChem*, 2022, **15**(4), e202102220, DOI: **10.1002/cssc.202102220**.

14 O. Mukhan, J.-S. Yun, H. Munakata, K. Kanamura and S.-S. Kim, Quantification of the Carbon-Coating Effect on the Interfacial Behavior of Graphite Single Particles, *ACS Omega*, 2024, **9**(3), 4004–4012, DOI: **10.1021/acsomega.3c08681**.

15 J. S. Yun, O. Mukhan, W. Cho, J. S. Yu, H. Munakata, K. Kanamura and S. S. Kim, How to Consider the Interfacial Phenomenon in All-Solid-State Batteries? – Quantitative Analysis using μ-Cavity Electrode, *Adv. Sustainable Syst.*, 2024, **8**(1), 2300297, DOI: **10.1002/adsu.202300297**.

16 Z. Cui, X. Li, X. Bai, X. Ren and X. Ou, A comprehensive review of foreign-ion doping and recent achievements for nickel-rich cathode materials, *Energy Storage Mater.*, 2023, **57**, 14–43, DOI: **10.1016/j.ensm.2023.02.003**.

17 K. J. Park, H. G. Jung, L. Y. Kuo, P. Kaghazchi, C. S. Yoon and Y. K. Sun, Improved Cycling Stability of Li $[Ni_{0.90}Co_{0.05}Mn_{0.05}]O_2$ Through Microstructure Modification by Boron Doping for Li-Ion Batteries, *Adv. Energy Mater.*, 2018, **8**(25), 1801202, DOI: **10.1002/aenm.201801202**.

18 K.-S. Lee, S.-T. Myung, K. Amine, H. Yashiro and Y.-K. Sun, Structural and Electrochemical Properties of Layered Li $[Ni_{1-2x}Co_xMn_x]O_2$ (x=0.1–0.3) Positive Electrode Materials for Li-Ion Batteries, *J. Electrochem. Soc.*, 2007, **154**, A971, DOI: **10.1149/1.2769831**.

19 S. Wang, X. Zhou, T. Zhao, J. Peng, B. Zhang, W. Xing, M. Zuo, P. Zhang, W. Fan, G. Lv, W. Hua and W. Xiang, Precise regulation of particle orientation for Ni-rich cathodes with ultra-long cycle life, *Nano Energy*, 2024, **129**(Part A), 110008, DOI: **10.1016/j.nanoen.2024.110008**.

20 G. T. Park, N. Y. Park, T. C. Noh, B. Namkoong, H. H. Ryu, J. Y. Shin, T. Beierling, C. S. Yoon and Y. K. Sun, High-performance Ni-rich $Li[Ni_{0.9-x}Co_{0.1}Al_x]O_2$ cathodes via multistage microstructural tailoring from hydroxide precursor to the lithiated oxide, *Energy Environ. Sci.*, 2021, **14**, 5084–5095, DOI: **10.1039/d1ee01773j**.

21 U. H. Kim, D. W. Jun, K. J. Park, Q. Zhang, P. Kaghazchi, D. Aurbach, D. T. Major, G. Goobes, M. Dixit, N. Leifer, C. M. Wang, P. Yan, D. Ahn, K. H. Kim, C. S. Yoon and Y. K. Sun, Pushing the limit of layered transition metal oxide cathodes for high-energy density rechargeable Li ion batteries, *Energy Environ. Sci.*, 2018, **11**, 1271–1279, DOI: **10.1039/c8ee00227d**.

22 T. Weigel, F. Schipper, E. M. Erickson, F. A. Susai, B. Markovsky and D. Aurbach, Structural and Electrochemical Aspects of $LiNi_{0.8}Co_{0.1}Mn_{0.1}O_2$ Cathode Materials Doped by Various Cations, *ACS Energy Lett.*, 2019, **4**, 508–516, DOI: **10.1021/acsenergylett.8b02302**.

23 Z. Zhu, A. Gao, Y. Liang, F. Yi, T. Meng, J. Ling, J. Hao and D. Shu, Dual-Functional Tungsten Boosted Lithium-Ion Diffusion and Structural Integrity of $LiNi_{0.8}Co_{0.1}Mn_{0.1}O_2$ Cathodes for High Performance Lithium-Ion Batteries, *ACS Sustainable Chem. Eng.*, 2022, **10**, 50–60, DOI: **10.1021/acssuschemeng.1c04076**.

24 E. Trevisanello, R. Ruess, G. Conforto, F. H. Richter and J. Janek, Polycrystalline and Single Crystalline NCM Cathode Materials—Quantifying Particle Cracking, Active Surface Area, and Lithium Diffusion, *Adv. Energy Mater.*, 2021, **11**(18), 2003400, DOI: **10.1002/aenm.202003400**.

25 P. Laine, M. Hietaniemi, J. Välikangas, T. Kauppinen, P. Tynjälä, T. Hu, S. Wang, H. Singh and L. Ulla, Co-precipitation of Mg-doped $Ni_{0.8}Co_{0.1}Mn_{0.1}(OH)_2$: effect of magnesium doping and washing on the battery cell performance, *Dalton Trans.*, 2023, **52**, 1413–1424, DOI: **10.1039/d2dt02246j**.

26 Z. Wu, *et al.*, Anionic-surfactant-assisted synthesis of $Ni_{0.8}Co_{0.1}Mn_{0.1}(OH)_2$ as precursors of high-performance cathode materials for lithium-ion batteries, *J. Power Sources*, 2024, **615**, 235092, DOI: **10.1016/j.jpowsour.2024.235092**.

27 Z. Wu, *et al.*, Improving electrochemical performance of NCM811 cathodes for lithium-ion batteries via consistently arranging the hexagonal nanosheets with exposed {104} facets., *Ceram. Int.*, 2022, **48**(12), 17279–17288, DOI: **10.1016/j.ceramint.2022.02.289**.

28 K. Ben-Kamel, *et al.*, Study of the local structure of $LiNi_{0.33+\delta}Mn_{0.33+\delta}Co_{0.33-2\delta}O_2$ ($0.025 \leq \delta \leq 0.075$) oxides, *J. Alloys Compd.*, 2012, **528**, 91–98.

29 H. Porthault, *et al.*, Raman study of the spinel-to-layered phase transformation in sol–gel LiCoO2 cathode powders as a function of the post-annealing temperature, *Vib. Spectrosc.*, 2012, **62**, 152–158.

30 X. Li, *et al.*, Improved rate capability of a $LiNi_{1/3}Co_{1/3}Mn_{1/3}O_2$/CNT/graphene hybrid material for Li-ion batteries, *RSC Adv.*, 2017, **7**(39), 24359–24367.

31 X. Li, *et al.*, *In situ* carbon coating to enhance the rate capability of the $Li_4Ti_5O_{12}$ anode material and suppress the electrolyte reduction decomposition on the electrode, *Electrochim. Acta*, 2016, **190**, 69–75.

32 J.-H. Park, *et al.*, A novel ion-conductive protection skin based on polyimide gel polymer electrolyte: application to nanoscale coating layer of high voltage $LiNi_{1/3}Co_{1/3}Mn_{1/3}O_2$ cathode materials for lithium-ion batteries, *J. Mater. Chem.*, 2012, **22**(25), 12574–12581.

33 C. M. Julien and A. Mauger, In situ Raman analyses of electrode materials for Li-ion batteries, *AIMS Mater. Sci.*, 2018, **5**(4), 650–698.

34 A. P. Ayanwale, B. L. Estrada-Capetillo and S. Y. Reyes-López, Evaluation of antifungal activity by mixed oxide metallic nanocomposite against *Candida* spp., *Processes*, 2021, **9**(5), 773.

35 Y. Chu, Y. Mu, L. Zou, F. Wu, L. Yang, Y. Feng and L. Zeng, Oxygen Release in Ni-Rich Layered Cathode for Lithium-Ion Batteries: Mechanisms and Mitigating Strategies, *ChemElectroChem*, 2024, **11**(14), e202300653, DOI: **10.1002/celc.202300653**.

36 K. Ando, Y. Yamada, K. Nishikawa, T. Matsuda, D. Imamura and K. Kanamura, Degradation Analysis of $LiNi_{0.8}Co_{0.15}Al_{0.05}O_2$ for Cathode Material of Lithium-Ion Battery Using Single-Particle Measurement, *ACS Appl. Energy Mater.*, 2018, **1**, 4536–4544, DOI: **10.1021/acsaem.8b00612**.

37 M. Malik, K. H. Chan and G. Azimi, Review on the synthesis of $LiNi_xMn_yCo_{1-x-y}O_2$ (NMC) cathodes for lithium-ion batteries, *Mater. Today Energy*, 2022, **28**, 101066, DOI: **10.1016/j.mtener.2022.101066**.

38 A. J. Bard and L. R. Faulkner, *Electrochemical Methods: Fundamentals and Applications*, John Wiley & Sons, New York, 2nd edn, 1980. **https://www.wiley.com/en-kr/Electrochemical+Methods%3A+Fundamentals+and+Applications%2C+2nd+Edition-p-9780471043720**.

39 K. Ando, M. Tsuta and K. Kanamura, Impact of active material ion diffusion coefficient on overpotential in lithium-ion batteries, *J. Electroanal. Chem.*, 2023, **948**, 117802, DOI: **10.1016/j.jelechem.2023.117802**.